symmetry

MDPI

Article

Determination of Spinel Content in Cycled $Li_{1.2}Ni_{0.13}Mn_{0.54}Co_{0.13}O_2$ Using Three-Dimensional Electron Diffraction and Precession Electron Diffraction

Matthias Quintelier [1], Tyché Perkisas [2], Romy Poppe [1], Maria Batuk [1], Mylene Hendrickx [1] and Joke Hadermann [1,*]

[1] EMAT, Department of Physics, University of Antwerp, 2020 Antwerp, Belgium; matthias.quintelier@uantwerpen.be (M.Q.); romy.poppe@uantwerpen.be (R.P.); maria.batuk@uantwerpen.be (M.B.); Mylene.hendrickx@uantwerpen.be (M.H.)

[2] Department of Engineering Management, Faculty of Business and Economics, University of Antwerp, 2000 Antwerp, Belgium; tyche.perkisas@uantwerpen.be

* Correspondence: joke.hadermann@uantwerpen.be

Abstract: Among lithium battery cathode materials, $Li_{1.2}Ni_{0.13}Mn_{0.54}Co_{0.13}O_2$ (LR-NMC) has a high theoretical capacity, but suffers from voltage and capacity fade during cycling. This is partially ascribed to transition metal cation migration, which involves the local transformation of the honeycomb layered structure to spinel-like nano-domains. Determination of the honeycomb layered/spinel phase ratio from powder X-ray diffraction data is hindered by the nanoscale of the functional material and the domains, diverse types of twinning, stacking faults, and the possible presence of the rock salt phase. Determining the phase ratio from transmission electron microscopy imaging can only be done for thin regions near the surfaces of the crystals, and the intense beam that is needed for imaging induces the same transformation to spinel as cycling does. In this article, it is demonstrated that the low electron dose sufficient for electron diffraction allows the collection of data without inducing a phase transformation. Using calculated electron diffraction patterns, we demonstrate that it is possible to determine the volume ratio of the different phases in the particles using a pair-wise comparison of the intensities of the reflections. Using this method, the volume ratio of spinel structure to honeycomb layered structure is determined for a submicron sized crystal from experimental three-dimensional electron diffraction (3D ED) and precession electron diffraction (PED) data. Both twinning and the possible presence of the rock salt phase are taken into account. After 150 charge–discharge cycles, 4% of the volume in LR-NMC particles was transformed irreversibly from the honeycomb layered structure to the spinel structure. The proposed method would be applicable to other multi-phase materials as well.

Keywords: 3D ED; PED; NMC; phase ratio; battery

Citation: Quintelier, M.; Perkisas, T.; Poppe, R.; Batuk, M.; Hendrickx, M.; Hadermann, J. Determination of Spinel Content in Cycled $Li_{1.2}Ni_{0.13}Mn_{0.54}Co_{0.13}O_2$ Using Three-Dimensional Electron Diffraction and Precession Electron Diffraction. *Symmetry* **2021**, *13*, 1989. https://doi.org/10.3390/sym13111989

Academic Editors: Arturo Ponce-Pedraza, Partha Pratim Das, Enrico Mugnaioli and Stavros Nicolopoulos

Received: 16 August 2021
Accepted: 13 October 2021
Published: 20 October 2021

1. Introduction

Battery cathode materials based on $Li_{1+\delta}(Ni_{1-x-y}Mn_xCo_y)_{1+\delta}O_2$ are widely investigated in various compositions for the different advantages that specific Li:Ni:Mn:Co ratios can give in capacity and power density. Voltage fade and capacity fade are not yet optimally subdued, partially due to the creation of secondary phases during cycling [1–4]. Their parent structure is a layered $LiCoO_2$ type, and in the case of lithium-rich compounds ($\delta > 0$)—such as the $Li_{1.2}Ni_{0.13}Mn_{0.54}Co_{0.13}O_2$ (LR-NMC) studied in this paper—there is a honeycomb order between the lithium atoms and the transition metal atoms in the transition metal layers (Figure 1a). Upon cycling, some of the transition metal atoms migrate into the octahedral positions within the lithium layers via the tetrahedral positions, which can occur in an ordered manner, creating a spinel structure locally [1,5] (Figure 1c). There can also be a further transformation to a rock salt type structure with disorder between the

lithium atoms and the transition metal atoms [6] (Figure 1d). Furthermore, surface layers with different compositions, both amorphous and crystalline, can be formed [7].

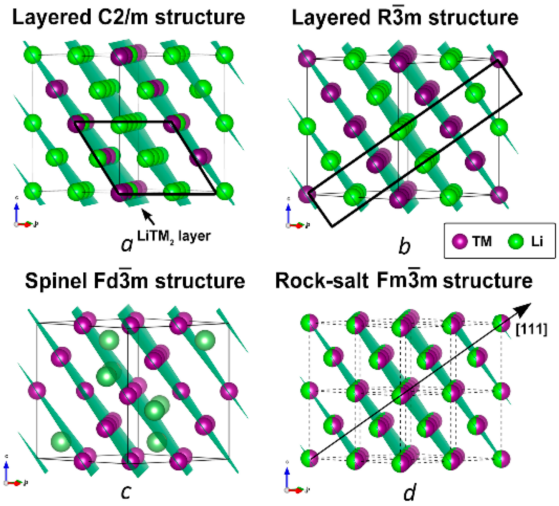

Figure 1. Crystal structure of $Li_{1.2}Ni_{0.13}Mn_{0.54}Co_{0.13}O_2$ (LR-NMC). In pristine LR-NMC, (**a**) there is a honeycomb order between the lithium atoms and the transition metal atoms in the transition metal layers, compared to the layered $LiCoO_2$ type structure in (**b**). During cycling, a spinel type structure (**c**) and a rock salt type structure (**d**) can be formed. The green and purple atoms represent Li and transition metals (TM = Ni, Mn, Co), respectively. For clarity, oxygen atoms are not shown.

The complex formation of secondary phases upon cycling is easiest to investigate by transmission electron microscopy (TEM), as this allows the direction observation of the structure at atomic resolution using different high-resolution imaging techniques [4,7,8]. However, it has been demonstrated that these compounds are sensitive to the electron beam, and imaging these particles has the same effect of turning the layered structure into a spinel structure [8–10]. Because of this, it is difficult to conclude that a certain change in the structure is due to cycling and not due to the electron beam. Moreover, it has been shown that twins originating from $Fm\bar{3}m$ rock salt type structure to $R\bar{3}m$ layered structure (Figure 1d,b) symmetry lowering during synthesis can easily be mistaken for the occurrence of spinel or rock salt phases when relying only on images [11–13].

From TEM imaging, the spinel structure is observed at the surface of the particles [1]. In situ synchrotron X-ray diffraction showed that there are also transition metals in the octahedral positions of the lithium layers (corresponding to transition metal positions in spinel but not in layered phases) in the bulk of the particles [2]. X-ray powder diffraction needs modelling and the implementation of various assumptions [2]. However, single-crystal X-ray diffraction cannot be used to determine the evolution of the structure because the lithium diffusion paths are too long to give a representative behavior in single crystals of a large enough size for single crystal X-ray diffraction. TEM imaging techniques are inadequate to detect the occurrence of spinel in the bulk of the crystals because the thickness of the crystals prevents the obtaining of clear images of bulk areas.

Therefore, we suggest using electron diffraction instead. In contrast to single-crystal X-ray or neutron diffraction, single-crystal electron diffraction can be done on submicron-sized crystals, which is the size used in battery cathode materials. When compared to TEM imaging, electron diffraction can readily distinguish whether extra reflections are due to twinning or due to the formation of the spinel phase [11–13]. Furthermore, electron diffraction requires lower beam intensities while still giving access to information at the level of atom coordinates, even of the lithium ions [14–18].

Still, whereas the amount of transition metal atoms in tetrahedral positions can be obtained using least squares refinement from three-dimensional electron diffraction (3D ED) data for Ni-rich $LiNi_{1-x-y}Mn_xCo_yO_2$ compounds [19], least squares refinement of

LR-NMC from 3D ED data has not yet been successful due to the presence of strong diffuse streaks along the c* axis in the electron diffraction patterns. The intensity maxima along the diffuse streaks are caused by twins originating from extra $R\bar{3}m$ (Figure 1b) to $C2/m$ (Figure 1a) symmetry lowering. The diffuse streaked character of these reflections is due to the nanoscale stacking of slabs of the different twins. When the samples are cycled, the occurrence of spinel and rock salt phases further complicates the refinement. Refining the phase ratio of spinel to honeycomb layered structure from the intensity profile of the diffuse streaks [20–23] is not a possibility for LR-NMC, since the spinel and honeycomb layered characteristic reflections form separate rows.

In this paper, we demonstrate the difference in sensitivity to the electron beam between pristine and charged LR-NMC type materials, demonstrate that it is possible to obtain electron diffraction patterns without introducing extra spinel, and provide a strategy to determine the ratio between the different phases present in a particle from 3D ED when least squares refinement does not give a solution due to a complex microstructure. Using this method, we determine the percentage spinel present in the volume of a submicron sized LR-NMC crystal in the discharged state after it has been cycled 150 times.

2. Materials and Methods

The details on the synthesis and cycling of $Li_{1.2}Ni_{0.13}Mn_{0.54}Co_{0.13}O_2$ (LR-NMC) and $Li_{1.2}Ni_{0.13}Mn_{0.513}Co_{0.13}Sn_{0.027}O_2$ (Sn-doped LR-NMC) are given in reference [24]. Both materials were galvanostatically cycled between 3.0 and 4.55 V vs. Li/Li+ at C-rates of C/20 during the initial two cycles and C/10 during the subsequent cycles. The effect of the electron beam was tested on both pristine and one time charged Sn-doped LR-NMC. For the application of the phase ratio determination method explained in this paper, a 150-times cycled LR-NMC sample was used in the discharged state.

All electron diffraction patterns were taken on Tecnai transmission electron microscope (Thermo Fisher, Eindhoven, The Netherlands) operated at 200 kV. The experiments with charged and discharged particles were done using a vacuum transfer holder (Gatan, Pleasanton, CA, USA) to prevent exposing the particles to air; the pristine sample was studied using a conventional double tilt holder (Gatan, Pleasanton, CA, USA).

In-zone electron diffraction patterns were acquired with precession electron diffraction (PED) using a Digistar precession attachment (Nanomegas, Brussels, Belgium), with a precession angle of 1°. Three-dimensional electron diffraction (3D ED) data were acquired with the manual electron diffraction tomography method, at intervals of 1° tilt. All electron diffraction patterns were recorded using an FEI Eagle 2k CCD camera (Thermo Fisher, Eindhoven, The Netherlands).

For validation of the method, in-zone electron diffraction patterns of core-shell particles were calculated using DISCUS (version 6.00.02) [25,26].

The reconstruction of the reciprocal space sections and the extraction of the intensities of the reflections were done using PETS (version 2.0) [27,28]. For the experimental data, the intensities were integrated using the fit profile option. For the data calculated in DISCUS, the intensities were integrated using the maximum intensity option. The fit profile option applies corrections, such that the resulting intensities I in the (hkl, I)-lists agree with the formula $I(hkl) = F(hkl)F^*(hkl)$—with $F(hkl)$, the structure factor for electron scattering, and $F^*(hkl)$, its complex conjugate. The maximum intensity option does not apply corrections. As DISCUS calculates the intensities using $I(hkl) = F(hkl)F^*(hkl)$, no corrections should be applied for the analysis of the calculated data.

For the analysis of the intensity ratios from the (hkl, I)-lists, an in-house written Matlab code "Crystalblender" was used, which is available upon request. Refinements were done using JANA2006 (version 25/10/2015) [29]. Fitting of the histograms to acquire the mean value and standard deviation were done using Fityk (version 1.3.1) [30].

3. Results and Discussion

3.1. Effect of the Electron Beam on the Spinel Ratio in LR-NMC Battery Cathode Materials When Using Electron Diffraction

While the effect of the electron beam on the spinel content in $Li_{1.2}Ni_{0.13}Mn_{0.54}Co_{0.13}O_2$ (LR-NMC)-type materials has been well documented for TEM imaging techniques [8–10], no literature is available on the effect of electron diffraction on the amount of spinel. Electron diffraction can be performed with a good signal-to-noise ratio using much lower electron doses than TEM imaging [18,31–33]. Therefore, we first investigated the effect of the electron beam in electron diffraction setting using a pristine and a charged sample of the same material at different beam intensities. For this experiment, we used $Li_{1.2}Ni_{0.13}Mn_{0.513}Co_{0.13}Sn_{0.027}O_2$ (Sn-doped LR-NMC), which is a typical doped LR-NMC compound that rapidly transforms to the spinel phase under the electron beam conditions used for imaging [24]. If the particles can be illuminated by electron diffraction at appropriate intensities for a long enough time without the creation of the spinel phase, three-dimensional electron diffraction (3D ED) data can deliver reliable information on the change in spinel content due to charging and discharging.

To make a first visual evaluation during the ongoing experiment, we chose to observe $[010]_H = [0\bar{1}1]_{SP}$ (H—honeycomb layered phase, SP—spinel phase) in-zone electron diffraction patterns during irradiation (See Figure S1 for the relations between the different in-zone patterns based upon the transformation matrices described in Section 3.2). This zone includes lattice points, where reflections only occur in the presence of the spinel phase. We used particles that were almost in-zone and thus required only minimal orientation, to avoid as much irradiation as possible before the first in-zone pattern could be recorded. Since the particles did not show pronounced anisotropy, a small diameter should be associated with a small thickness. Therefore, we chose particles with a small diameter, around maximally 200 nm in diameter, to keep the contribution of dynamical scattering low. For typical lithium battery cathode materials, the kinematical approach in treating 3D ED or precession electron diffraction (PED) data is adequate, due to the low atomic number of the elements (inherent to battery requirements to keep the portable batteries as light as possible) [16,31–34]. A selected area aperture of 500 nm was used, which allowed the particles to fit completely in the aperture with some room for movement while still maintaining a sufficient quality signal-to-noise ratio, with as low as possible background from both the central beam and from diffraction on the amorphous carbon support. PED patterns were taken directly after in-zone orientation was obtained (Figure 2a,c). The particles were then irradiated using a beam with 45(14) $e^-/Å^2s$—similar to the intensity we normally use for 3D ED, where no special care needs to be taken concerning beam sensitivity, and similar to what is used for conventional selected area electron diffraction. PED patterns were then acquired every 5 min for 60 min. We saw no changes for either the pristine or the charged particles (Figure 2b,d). For the charged particles we then focused the electron beam to obtain a high intensity (1.1(4).10^4 $e^-/Å^2s$). The focused beam had the size of the particle, to ensure that the entire particle was homogeneously irradiated. During this irradiation, new PED patterns were taken every 5 min. Only with this higher electron dose rate did the spinel-only reflections appear after 20 min (Figure 2e) and keep increasing in intensity (Figure 2f). Thus, our data showed it was possible to acquire the necessary dataset for the determination of the spinel content present in the crystal without observably affecting it during at least 60 min, using normal electron diffraction settings. A manually obtained 3D ED series takes less than 60 min, and automated ones take only a few minutes [35–39], while an in zone PED pattern takes mainly the time necessary to orient the pattern. Therefore, 3D ED series and in-zone PED patterns can be obtained without affecting the spinel content. Note that for these LR-NMC materials it is not even necessary to use conditions such as those used for beam sensitive materials, as used for example by Palatinus et al. for hydrogen-containing materials [40], Kolb et al. for organics [41] or by Kodjikian et al. [42]—although this would also still be a possibility for ensuring a lower beam effect if deemed necessary.

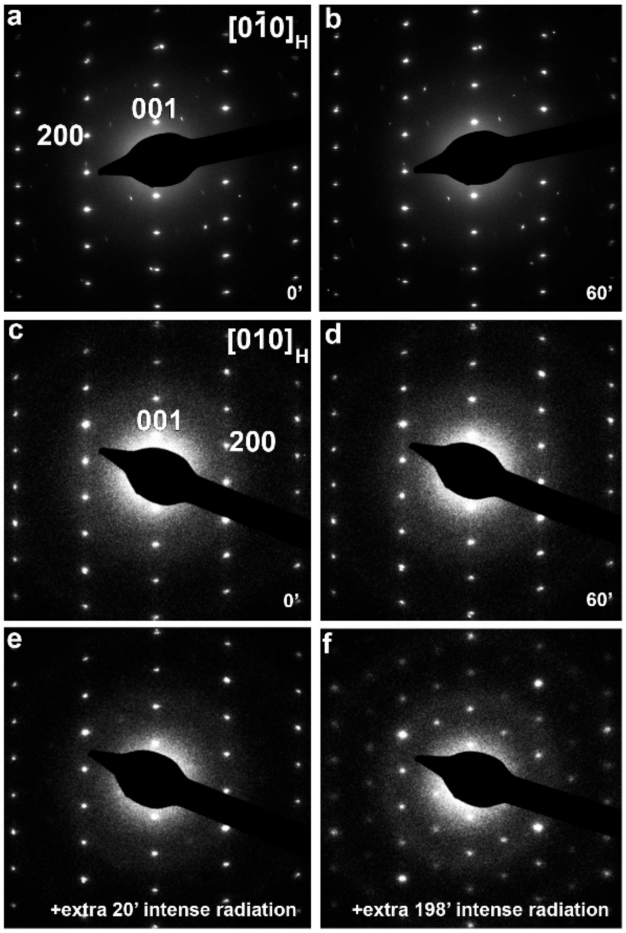

Figure 2. Selected area precession electron diffraction (PED) patterns of the $[0\bar{1}0]_H$ zone of a pristine particle after (**a**) 0 min and (**b**) 60 min at electron dose rate of 45(14) e/Å^{2}s, showing no change. PED patterns of the $[010]_H$ zone of a one-time charged particle after (**c**) 0 min and (**d**) 60 min at electron dose rate of 45(14) $e^-/Å^2$s, showing no change; (**e**) after an extra 20 min at electron dose rate 1.1(4).10^4 $e^-/Å^2$ s, weak reflections belonging to the spinel phase have appeared; (**f**) after 198 extra minutes at electron dose rate 1.1(4).10^4 $e^-/Å^2$ s, showing very clear reflections from the spinel phase. Slight differences in background intensity are due to adjustments of the total grey level interval for best visualization of all reflections.

3.2. Determination of the Amount of Spinel in a LR-NMC Submicron-Sized Crystal

Whereas we showed in the previous section that electron diffraction gives a reliable representation of the amount of spinel in LR-NMC crystals, quantification of the amount of spinel is far from routine. As explained in the introduction, the multitude of defects and phases in LR-NMC has so far prevented a refinement of the phase ratio or the occupancy of the positions from electron diffraction single crystal data. Refinements of the occupancies have been performed using powder X-ray diffraction, but need extensive modelling and assumptions [2].

Therefore, we propose to use the pair-wise intensity ratios of the reflections in electron diffraction data to obtain the phase ratio. For most reflection pairs, a certain intensity ratio will correspond to a unique phase ratio. Therefore, the phase ratio can be obtained from the intensity ratio. If such analysis was done based on conventional in-zone electron diffraction patterns, there would be several sources of errors—most importantly deviations in the intensities due to slight misorientation and deviations due to dynamical scattering. Therefore, we will use 3D ED data, for which the reflection intensities are integrated over several out-of-zone frames, which considerably reduces the dynamical contributions, and in-zone PED data, where the precession reduces dynamical scattering. We only studied

particles that fit entirely within the 200 nm selected area aperture as a criterium of their size, to further limit the dynamical scattering contribution to the intensities. The phase ratio is calculated by comparing the experimental intensity ratio with the theoretical intensity ratio curve calculated for varying spinel content. Each pair thus results in a contribution to the distribution of the experimental spinel content. The standard deviation σ_I of the intensities is taken into account by calculating the standard deviation of the experimentally determined spinel content using error propagation and building a normal distribution, with μ being the mean spinel content and σ its standard deviation. Thus, instead of comparing one value (the experimentally determined intensity ratio) with the (spinel content, intensity ratio) curve, an entire distribution is compared, resulting in a likewise distribution for the spinel content.

For obtaining a single (*hkl*, *I*)-list containing all reflections of both the spinel and the honeycomb layered phase, both unit cells need to be transformed into a common supercell. A similar procedure was used for indexing twins in 3D ED data [43].The supercell is only used to allow indexing of all reflections, after which the transformation matrices are used to calculate the structure factor per volume unit using the corresponding reflections in the original unit cells. This allows for the user to use the original cell's CIF files and not spend time developing CIF files for the supercell. The intensities are then calculated corresponding to a continuously changing phase ratio by parametrizing the structure factor using the phase's volume percentage x as:

$$\frac{F}{V} = x\,\frac{F_A}{V_A} + (1-x)\frac{F_B}{V_B} \tag{1}$$

with $F_{A(B)}$ the structure factor originating from phase $A(B)$, and $V_{A(B)}$ the volume of the respective unit cells $A(B)$, which leads to an intensity:

$$I = k\left|x\,\frac{F_A}{V_A} + (1-x)\frac{F_B}{V_B}\right|^2.V^2, \tag{2}$$

with k a scale factor depending on the thickness of the crystal and the beam intensity. The scale factor will be eliminated when taking the ratio of the intensities. Details on the derivation of this formula can be found in the Supplementary Materials. The relation of the basis vectors of the common supercell to the basis vectors of the honeycomb layered (H) unit cell and the spinel (SP) unit cell is indicated in Figure 3. The transformation matrices for both phases to this common supercell are:

$$P_{H\rightarrow super} = \begin{pmatrix} 1 & 1 & 1 \\ -1 & 1 & 0 \\ 0 & 0 & 3 \end{pmatrix} \tag{3}$$

$$P_{SP\rightarrow super} = \begin{pmatrix} 0.5 & 0.5 & -1 \\ 0.5 & -1 & -1 \\ -1 & 0.5 & -1 \end{pmatrix} \tag{4}$$

Note that this common supercell also allows the indexing of all rock salt reflections, since these overlap with spinel and honeycomb layered reflections, as the rock salt structure is the parent subcell of the honeycomb layered structure and the spinel structure (Figure 1). For clarity and comprehension, several calculated main zone electron diffraction patterns are included in Figure S1, showing next to each other the indices in honeycomb layered, spinel and rock salt structures, and in the common supercell. For the remainder of this paper, all indices will be given relative to the supercell axes, as indicated by the subscript S.

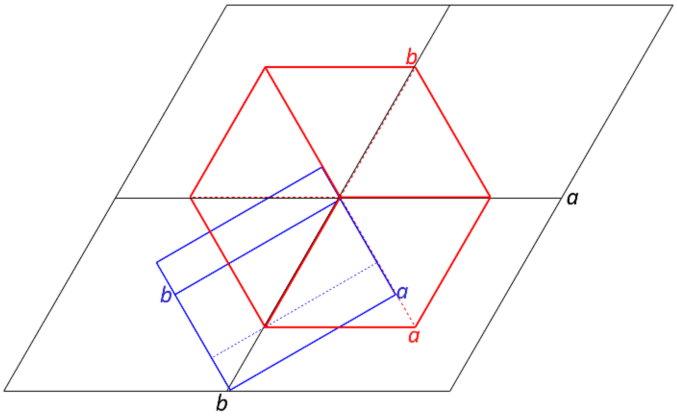

Figure 3. Relation between the basis vectors of the honeycomb layered structure (blue), the spinel structure (red) and the common supercell (black), projected along the c-axis of the supercell. The rock salt structure axes are the halved spinel axes. The labels a and b, indicating the basis vectors, are placed at the ends of the basis vectors, the origin is at the center of the scheme.

To test the approach, we used in-zone electron diffraction patterns calculated in DISCUS. Spherical core-shell particles with a honeycomb layered ($C2/m$) core [44] (ICSD 237940) and a spinel ($Fd\bar{3}m$) [45] (ICSD 40485) shell were modelled with varying ratios. For reasons of feasibility, no stacking faults or twinning were included in the model. All transition metals (Z_{Mn} = 25, Z_{Co} = 27, Z_{Ni} = 28) were approximated as Mn for the DISCUS calculations to avoid artefacts from the short-range transition metal order. To build a core-shell model in DISCUS, the cell parameters for both phases need to be identical. This was achieved by transforming both structures to the same common supercell as we used for the indexation of the experimental 3D ED series. Figure 4 shows the cross-section of a spherical crystal with 10 × 10 × 10 supercell unit cells and a spinel/honeycomb layered ratio of 50:50.

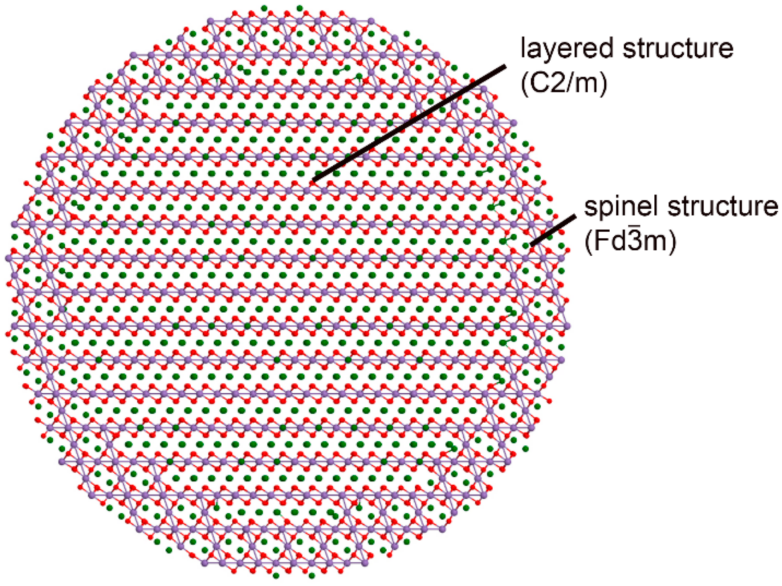

Figure 4. Cross-section of a spherical core-shell LR-NMC particle used for calculating electron diffraction patterns using DISCUS. The particle has a size of 10 × 10 × 10 supercell unit cells with a honeycomb layered core and a spinel shell. The spinel/honeycomb layered ratio used for the simulation of this particle is 50:50. Green, purple and red spheres represent lithium, transition metals and oxygen, respectively.

The $[\bar{1}10]_S$ (and $[100]_s$) electron diffraction patterns were calculated in DISCUS for a spinel content of 2, 5, 10, 20 and 50% (examples shown in Figure 5; Figure S2 for $[100]_S$). These patterns can be compared to Figure S1 for the origin of each reflection. Subsequently, the intensities of the reflections were extracted using PETS2 software [28] to get an (*hkl*, *I*)-list. Figure 6 shows the lattice points where PETS2 extracted the intensities using the supercell.

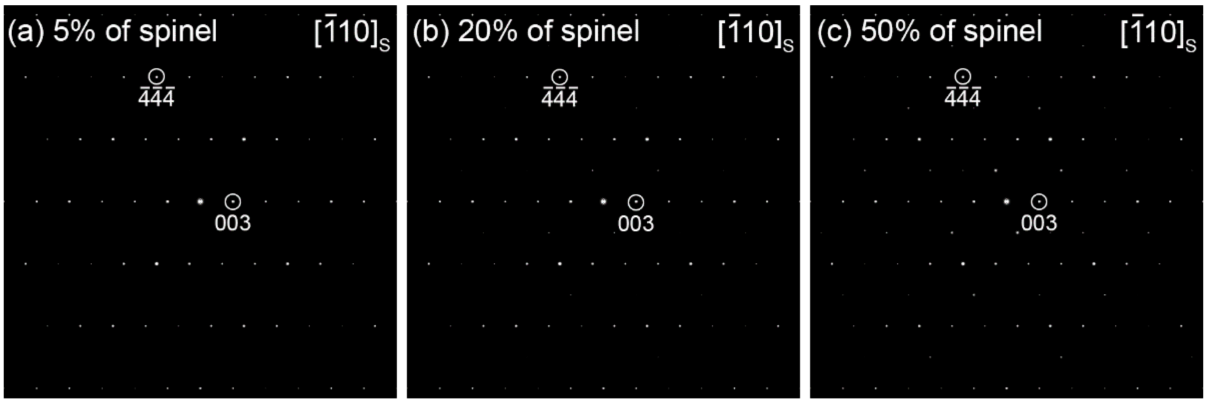

Figure 5. $[\bar{1}10]_S$ electron diffraction patterns calculated for, respectively, 5%, 20% and 50% of spinel, for a spherical crystal with $10 \times 10 \times 10$ supercell unit cells.

We tested different sets of reflection pairs: purely spinel over purely honeycomb layered, purely spinel over combined spinel and honeycomb layered, combined spinel and honeycomb layered over purely honeycomb layered, and combined spinel and honeycomb layered for both reflections (Figure S3). Only the pairs where one reflection was purely spinel and the other had a contribution from both the honeycomb layered and the spinel structure resulted in the correct spinel content. Using such reflection pairs, the (spinel content, intensity ratio) curve always shows a monotonous behavior that can be used for pinpointing which phase ratio corresponds to a certain intensity ratio. Reflection pairs in which both reflections have contributions from both phases often have multiple solutions for the spinel content, while for the other failing combinations, presumably, the effect of variations in spinel content is too small for reliable spinel content determination.

Figure 6 shows the (spinel content, intensity ratio) curve for an example reflection pair $\bar{1}\bar{1}5$:006, where $\bar{1}\bar{1}5$ is purely contributed by the spinel structure and 006 is a reflection common to both the spinel structure and the honeycomb layered structure. There is a good agreement of the curve obtained using the proposed equation $I = \mid x \frac{F_A}{V_A} + (1-x)\frac{F_B}{V_B} \mid^2$ to the discrete points obtained from Discus calculations for the core-shell particle.

The histograms corresponding to the datasets for the different spinel contents are shown in Figure 7, in which the frequency is the frequency of the corresponding x values where each reflection pair's intensity ratio can be represented with a distribution (taking its standard deviation into account). Drawing randomly from this distribution (weighing with their respective likelihood) thus gives rise to a distribution in x, as every one of the drawn values is mapped unto its corresponding x value. It was found that 100 drawings from the intensity ratio distribution was enough to represent it accurately—hence the factor of 100 between frequency and number of considered pairs. A clear peak is visible for the ratios of 2, 5, 10 and 20%, located at resp. 0.021(6), 0.05(1), 0.10(2) and 0.17(3). For the 50% spinel ratio, there are two peaks—the reason for this remains elusive to us—at 0.29(3) and 0.54(5). The numbers in the brackets are the half-width-half-maximum of the peaks. Thus, the proposed method gives reliable results for up to 20% spinel, which is well suited for the expected amount of spinel based on synchrotron X-ray data [2].

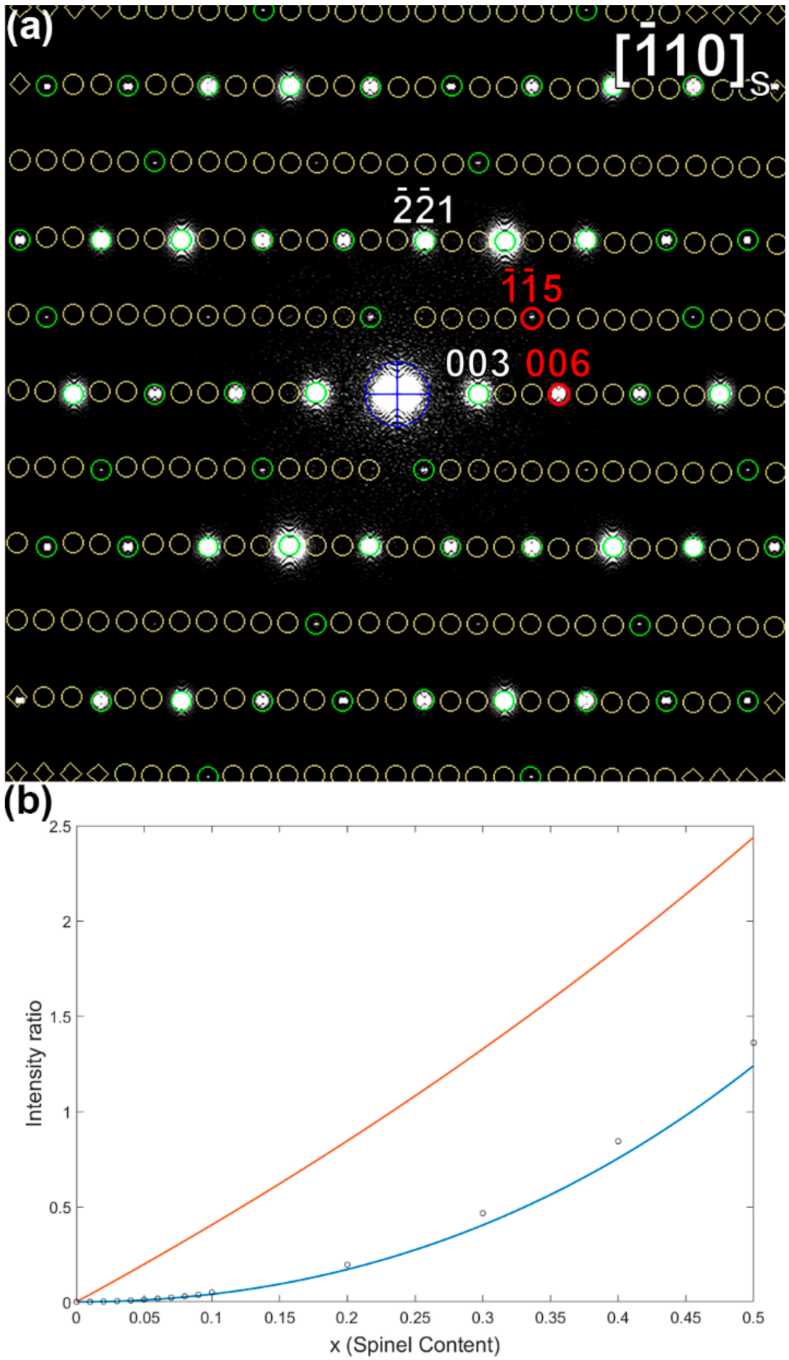

Figure 6. (**a**) Calculated $[\bar{1}10]_S$ zone for a spherical honeycomb layered–spinel core-shell particle with 2% of spinel. The circles indicate the positions of all reciprocal lattice points corresponding to the supercell ($I > 3\sigma$—green, $I < 3\sigma$—yellow). Red circles indicate the reflections used for the graph in (**b**), which shows as an example the intensity ratio of the $\overline{1}\overline{1}5$ to the 006 reflection versus the spinel content x (in percentage) as calculated in Discus (discrete dots), using Crystalblender with the formula $I = \mid x\ \frac{F_A}{V_A} + (1-x)\frac{F_B}{V_B}\ \mid^2$ implemented in this paper (blue line), and for comparison with the alternative formula $I = (x)I_A + (1-x)I_B$ (red line).

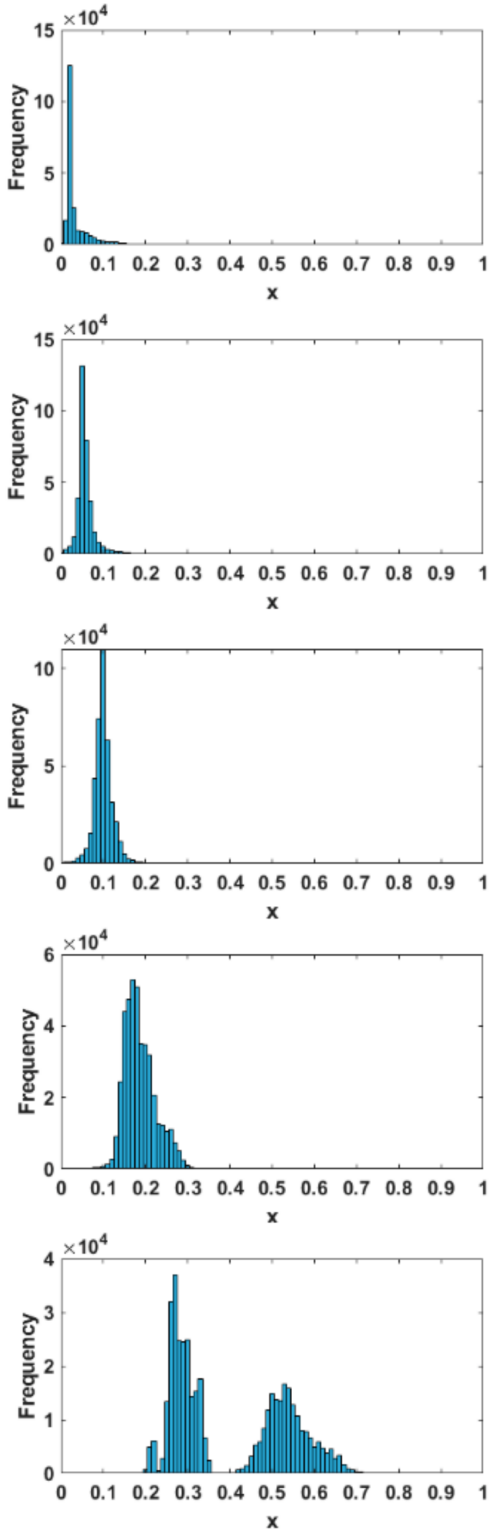

Figure 7. Histogram plots obtained using Crystalblender for the calculated DISCUS $[\bar{1}10]_S$ patterns with ratios of, from top to bottom, 2, 5, 10, 20 and 50% spinel. For these intensity ratios, the reflection pairs considered are all combinations of only reflections that only have $|F_A| > 0.0005$, $|F_B| < 0.0005$ for the numerator, and only reflections with $|F_A|$, $|F_A| > 0.0005$ for the denominator, and with h, k, l < 15. The frequency refers to the frequency of the x-values when the ratios are represented by 100 drawings from distributions of the intensity ratios with their standard deviations. The number of contributing pairs is the frequency divided by 100, as explained in the main text.

The calculated patterns are from idealized particles without twins, stacking faults, or rock salt structure contributions. This allows us to also attempt a conventional refinement to compare the results. The same (*hkl*, *I*)-lists were used as input for the refinement using JANA2006 [29]. We first attempted a two-phase least squares refinement with all structural parameters fixed to the literature values for the two phases, only refining the amount of the different phases and the scale factors. The refinement converged to incorrect, lower spinel contents (e.g., 1.1% instead of 10% of spinel, 4.9% instead of 20% of spinel and 32.8% instead of 50% of spinel, Table S1). An explanation for this can be found in the assumption in the least squares refinement that the intensities are due to separate crystals of the two phases, with the intensities being the sum of the separate intensities. However, in the core-shell particles, modelled after real observations made for LR-NMC cycled particles, both phases are present in the same particle. In our pair-wise intensity ratio approach, we have translated this into a contribution of both phases into the structure factor (Equation (5)) instead of a contribution only at the level of the intensities (Equation (6)). As described in Section 3.2, this results in intensities of supercell reflections as according to:

$$I = | \, x \, \frac{F_A}{V_A} + (1 - x) \frac{F_B}{V_B} |^2 \tag{5}$$

instead of:

$$I = (x)I_A + (1 - x)I_B, \tag{6}$$

which gives a resulting combined intensity I that is closer to that of a core-shell particle. As can be seen on Figure 6b, using Equation (6; red line) would result in lower apparent spinel contents than Equation (5; blue line) for the same intensity ratios.

Next, we attempted to refine the phase ratio using mixed occupancies in the supercell. This was not successful, as the number of refinable parameters was too high for the small number of reflections present in the single in-zone patterns. As a result, the refinement did not converge. Since this method assumes mixing of the phases at the structure factor level, we would expect that the least squares refinement of the occupancies would result in the correct spinel content. Unfortunately, simulating a full 3D ED series with the core-shell model in DISCUS to have sufficient reflections for the number of refinable parameters was not feasible.

Finally, the same ratio used as input could be successfully retrieved (although not by a real "refinement") by comparing the R factors for the agreement of the intensities for different fixed occupancies, leaving only the scale factors as refinable. Supercell models for 0–100% of spinel content with steps of 1% were created and tested versus the intensities obtained from the calculated diffraction patterns. This allowed us to pinpoint the correct phase ratio, as shown for example in Figure 8. In the case of the $[100]_S$ zone, the determined ratio was correct for 2, 5 and 10% of spinel, whereas for 20 and 50% the refined ratio was smaller than the correct one. Compared with the method based on pair-wise intensities, this phase ratio determination using the R factors demanded considerably more time and handling.

Thus, for calculated data, the pair-wise comparison of intensities and a search for the lowest R-factor using fixed-ratio input models gave comparable and correct results for the spinel contents of the two-phase honeycomb layered-spinel crystals up to, respectively, 20% and 10%, whereas two-phase least squares refinement with fixed structures gave too-low spinel contents.

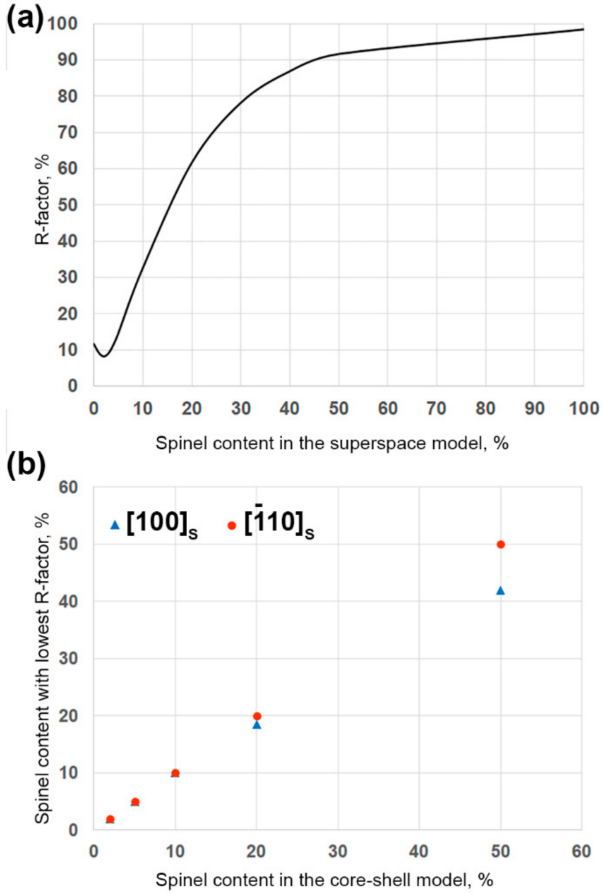

Figure 8. Results for least squares refinement using models with fixed ratios. (**a**) R factors obtained for the 2% spinel model. (**b**) Spinel contents with lowest R factor for the different $[100]_S$ and $[\bar{1}10]_S$ patterns with different spinel contents simulated in DISCUS.

3.3. Application to Experimental Data

We applied the phase ratio determination by pair-wise comparison of intensities on both an in-zone $[100]_S$ PED pattern and a 3D ED series acquired on the same LR-NMC crystal that was 150 times cycled and left in the discharged state (Figure 9). In contrast to the diffraction patterns calculated from the core-shell particle in the previous section, cycled LR-NMC crystals might also contain the rock salt phase. Therefore, all (*hkl*, *I*)-lists were filtered in Excel to remove all reflections for which all *h*, *k* and *l* are even and simultaneously $h + k + l = 6n$ in the supercell indexation, which covers all rock salt structure reflections (this can be easily verified on Figure S1). We cannot remove possible residual rock salt contributions present in the other reflections by multiple scattering, and we assume this effect is negligible. Besides the rock salt phase, the cycled LR-NMC crystals we studied contained stacking faults and twins caused by $R\bar{3}m$ to $C2/m$ symmetry lowering (extra details on the twinning in this material can be found in the Supplementary Materials). In such cases, each reflection that is due to only the layered phase in the (*hkl*, *I*)-lists will always have a contribution from only one twin, while the reflections overlapping with spinel contain contributions from all twins together. The intensities contributed by the different twins to the listed *hkl* will be different because the actual *hkl* for those twins at those positions will differ. Therefore, we expanded the calculation to take into account those different intensities by splitting up the layered intensities to consist of 1/3 of each twin. The estimate of 1/3 is based on a visual interpretation of the [100] PED pattern and *0kl* section of the 3D ED data. Additionally, thermodynamically it is likely that the three twins occur in equal amounts. The results with and without taking the twinning into account are shown in Figure 10. Not taking the twins into account results in a histogram with multiple

peaks (Figure 10), while introducing the twins results in a clear single peak with only slight signs of a shoulder and tail. The latter are probably due to residual contributions from the two other twins if our equal distribution was not perfectly valid, as well as due to residual dynamical scattering. Dynamical scattering will redistribute the intensity from the strong reflections to the weaker reflections. In electron diffraction patterns of LR-NMC, the strongest reflections are the reflections common to both honeycomb layered and spinel, while the reflections purely from the spinel structure are among the weakest. Dynamical scattering could thus increase the apparent spinel content from many reflection pairs. A third possible contributor to the shoulder and tail is the presence of a small number of twins of the type created by $Fm\bar{3}m$ to $R\bar{3}m$ symmetry lowering during synthesis (more details in the Supplementary Materials).

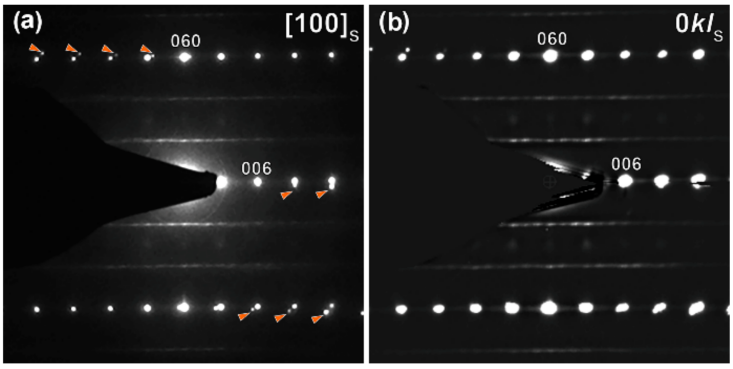

Figure 9. (**a**) $[100]_S$ in-zone PED pattern and (**b**) 0*kl* section of a 3D ED series of the same 150× cycled discharged LR-NMC crystal used for the phase ratio determination (orange arrowheads point to the reflections from another domain).

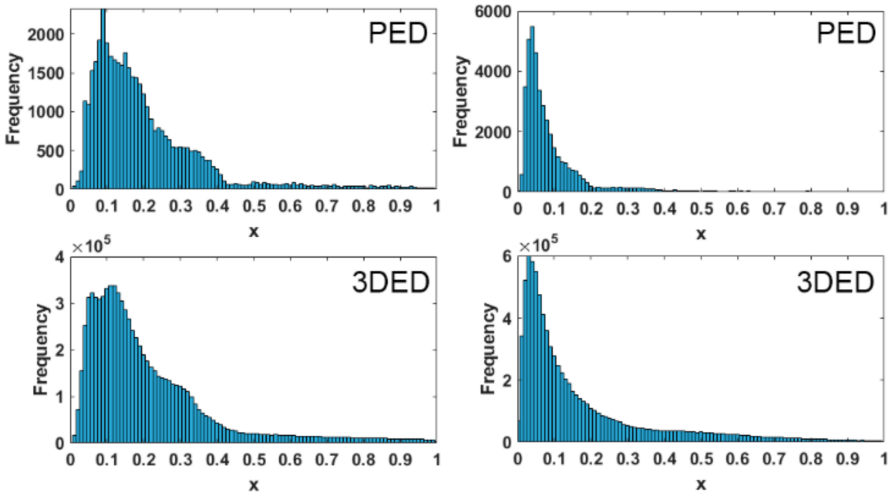

Figure 10. Histograms showing the estimated spinel content in 150× cycled discharged LR-NMC crystals. The left-side histograms show the results when including only a single honeycomb layered twin, while the right-side histograms show the improved results by including also the 120° and 240° rotation twins. The results are shown for both the PED data (**top**) and 3D ED data (**bottom**). The number of pairs contributing to each histogram bar is the frequency divided by 100.

For both the 3D ED data and the in-zone PED data, the highest peaks on the resulting histograms are best fitted using Gaussian peaks complemented by two extra smaller Gaussian peaks at higher x value describing the shoulders and tail. For both the PED in-zone data and the 3D ED data, the fit results in a peak at x = 0.04 with a half-width-half-maximum of 0.04 and a height resp. of 6418 (64 reflection pairs) and 1,069,885 (10,698 reflection pairs).

Long duration in situ synchrotron X-ray powder diffraction (SXRD) showed a continuous and irreversible increase in the number of transition metal atoms at the octahedral positions in the Li-layers–up to 5% after 100 cycles [2]. This is close to the 4% spinel content found in our study using particles that were 150 times cycled and observed in the discharged state. The slight difference might be due to the experimental errors but could also be due to transition metal atoms being at the octahedral positions in the Li-layers, but not in an ordered manner. These transition metal atoms would not contribute to spinel reflections (4% spinel from 3D ED and PED) but would contribute to the occupancy factor of those positions (5% from SXRD).

In our single-crystal electron diffraction data, the spinel reflections are present in the (*hkl*, *I*)-lists, supporting the observation from TEM imaging [1,5,25] that the spinel structure is present in the cycled LR-NMC particles. Since the conventional settings used for electron diffraction do not influence the formation of spinel, the 3D ED and PED data confirm that the spinel phase was formed during cycling and not induced by the electron beam.

The proposed method could also be applied to other combinations of phases as long as some reflections belong to only one of the two phases. For the current paper, the 3D ED data were acquired manually, but several methods are freely available that allow the taking of 3D ED series of many particles in a short time, such as fast electron diffraction tomography [38], ultra-fast electron diffraction tomography [46], fast-ADT [35], Instamatic [36,47] and InsteadMatic [37]—all part of the modern 3D ED family [14]. By combining such fast data collection with the simple phase ratio determination presented here, it should be possible to evaluate in a short time the phase ratio in a statistically relevant number of crystals or for the different stages of phase transformations taking place inside the transmission electron microscope during in situ experiments.

4. Conclusions

Electron diffraction data can be recorded without affecting the amount of spinel phase in $Li_{1.2}Ni_{0.13}Mn_{0.54}Co_{0.13}O_2$ (LR-NMC). This allows estimation of the relative volume of different phases in LR-NMC crystallites using the intensity ratios of reflections in precession electron diffraction (PED) patterns or in three-dimensional electron diffraction (3D ED) reconstructions. There has to be a careful consideration of the reflections that will be used, to have sufficient contributions from each phase and exclude other possibly present phases, and to exclude reflection pairs for which the intensity ratio does not show monotonous behavior.

The results of the application of this phase ratio determination method on experimental data obtained from 150 times cycled LR-NMC examined in the discharged state allowed the derivation of an amount of spinel in line with the amount of transition metal atoms found in octahedral positions in the lithium layer using synchrotron X-ray powder diffraction.

Supplementary Materials: The following are available online at https://www.mdpi.com/article/10.3390/sym13111989/s1, Figure S1: overview of the main zones (and relations between them) for all phases involved, indexed in original honeycomb layered, spinel and rock salt indices and in the supercell indices. Figure S2: $[100]_S$ electron diffraction patterns calculated for, respectively, 5%, 20% and 50% of spinel, for a spherical crystal with a size of 10 × 10 × 10 supercell unit cells. Figure S3: histograms of the resulting phase ratios for the calculated (*hkl*, *I*)-lists using different sets of reflection pairs. Clarification of the occurrence of twins in the compounds and how to recognize them. Figure S4: the relationship between the parent rock salt structure and the two common layered structures. Figure S5: equivalent zones in the cubic system. Figure S6: equivalent zones in the cubic system. Table S1: Details of the two-phase refinement of the spinel content in LR-NMC from ED patterns simulated using a spherical core-shell particle.

Author Contributions: Conceptualization, M.Q., T.P. and J.H.; methodology, T.P. and J.H.; software, T.P. and M.Q.; validation, R.P., M.B., M.Q., J.H.; formal analysis, all authors; investigation, M.Q., R.P., M.B.; resources, J.H.; writing—original draft preparation, M.Q. and J.H.; writing—review and

editing, all authors; supervision, J.H.; funding acquisition, J.H. All authors have read and agreed to the published version of the manuscript.

Funding: This research was funded by FWO, grant number G035619N and G040116N.

Institutional Review Board Statement: Not applicable.

Informed Consent Statement: Not applicable.

Data Availability Statement: The (*hkl*, *I*)-lists obtained from 3D ED and PED data are available on Zenodo at 10.5281/zenodo.5175929, accessed on 10 August 2021.

Acknowledgments: We thank Stefano Canossa, Daphne Vandemeulebroucke and Saleh Gholam for fruitful discussions.

Conflicts of Interest: The authors declare no conflict of interest. The funders had no role in the design of the study; in the collection, analyses, or interpretation of data; in the writing of the manuscript, or in the decision to publish the results.

References

1. Genevois, C.; Koga, H.; Croguennec, L.; Ménétrier, M.; Delmas, C.; Weill, F. Insight into the atomic structure of cycled lithium-rich layered oxide $Li_{1.20}Mn_{0.54}Co_{0.13}Ni_{0.13}O_2$ using HAADF STEM and electron nanodiffraction. *J. Phys. Chem. C* **2015**, *119*, 75–83. [CrossRef]
2. Kleiner, K.; Strehle, B.; Baker, A.R.; Day, S.J.; Tang, C.C.; Buchberger, I.; Chesneau, F.-F.; Gasteiger, H.A.; Piana, M. Origin of High Capacity and Poor Cycling Stability of Li-Rich Layered Oxides: A Long-Duration in Situ Synchrotron Powder Diffraction Study. *Chem. Mater.* **2018**, *30*, 3656–3667. [CrossRef]
3. Zhan, C.; Wu, T.; Lu, J.; Amine, K. Dissolution, migration, and deposition of transition metal ions in Li-ion batteries exemplified by Mn-based cathodes-A critical review. *Energy Environ. Sci.* **2018**, *11*, 243–257. [CrossRef]
4. Fan, Y.; Zhang, W.; Zhao, Y.; Guo, Z.; Cai, Q. Fundamental understanding and practical challenges of lithium-rich oxide cathode materials: Layered and disordered-rocksalt structure. *Energy Storage Mater.* **2021**, *40*, 51–71. [CrossRef]
5. Pimenta, V.; Sathiya, M.; Batuk, D.; Abakumov, A.M.; Giaume, D.; Cassaignon, S.; Larcher, D.; Tarascon, J.M. Synthesis of Li-Rich NMC: A Comprehensive Study. *Chem. Mater.* **2017**, *29*, 9923–9936. [CrossRef]
6. McCalla, E.; Abakumov, A.M.; Saubanere, M.; Foix, D.; Berg, E.J.; Rousse, G.; Doublet, M.-L.M.L.; Gonbeau, D.; Novak, P.; Van Tendeloo, G.; et al. Visualization of O-O peroxo-like dimers in high-capacity layered oxides for Li-ion batteries. *Science* **2015**, *350*, 1516–1521. [CrossRef]
7. Mauger, A.; Julien, C. Surface modifications of electrode materials for lithium-ion batteries: Status and trends. *Ionics* **2014**, *20*, 751–787. [CrossRef]
8. Lu, P.; Yan, P.; Romero, E.; Spoerke, E.D.; Zhang, J.G.; Wang, C.M. Observation of electron-beam-induced phase evolution mimicking the effect of the charge-discharge cycle in Li-rich layered cathode materials used for Li ion batteries. *Chem. Mater.* **2015**, *27*, 1375–1380. [CrossRef]
9. Lin, F.; Markus, I.M.; Nordlund, D.; Weng, T.-C.; Asta, M.D.; Xin, H.L.; Doeff, M.M. Surface reconstruction and chemical evolution of stoichiometric layered cathode materials for lithium-ion batteries. *Nat. Commun.* **2014**, *5*, 3529. [CrossRef] [PubMed]
10. Lin, F.; Markus, I.M.; Doeff, M.M.; Xin, H.L. Chemical and structural stability of lithium-ion battery electrode materials under electron beam. *Sci. Rep.* **2014**, *4*, 5694. [CrossRef] [PubMed]
11. Shukla, A.K.; Ramasse, Q.M.; Ophus, C.; Duncan, H.; Hage, F.; Chen, G. Unravelling structural ambiguities in lithium- and manganese-rich transition metal oxides. *Nat. Commun.* **2015**, *6*, 1–9. [CrossRef] [PubMed]
12. Jarvis, K.A.; Wang, C.C.; Knight, J.C.; Rabenberg, L.; Manthiram, A.; Ferreira, P.J. Formation and effect of orientation domains in layered oxide cathodes of lithium-ion batteries. *Acta Mater.* **2016**, *108*, 264–270. [CrossRef]
13. Jarvis, K.A.; Deng, Z.; Allard, L.F.; Manthiram, A.; Ferreira, P.J. Understanding structural defects in lithium-rich layered oxide cathodes. *J. Mater. Chem.* **2012**, *22*, 11550–11555. [CrossRef]
14. Gemmi, M.; Mugnaioli, E.; Gorelik, T.E.; Kolb, U.; Palatinus, L.; Boullay, P.; Hovmöller, S.; Abrahams, J.P. 3D electron diffraction: The nanocrystallography revolution. *ACS Cent. Sci.* **2019**, *5*, 1315–1329. [CrossRef] [PubMed]
15. Palatinus, L.; Corrêa, C.A.; Steciuk, G.; Jacob, D.; Roussel, P.; Boullay, P.; Klementová, M.; Gemmi, M.; Kopeček, J.; Domeneghetti, M.C.; et al. Structure refinement using precession electron diffraction tomography and dynamical diffraction: Tests on experimental data. *Acta Crystallogr. Sect. B Struct. Sci. Cryst. Eng. Mater.* **2015**, *71*, 740–751. [CrossRef] [PubMed]
16. Karakulina, O.M.; Demortière, A.; Dachraoui, W.; Abakumov, A.M.; Hadermann, J. In Situ Electron Diffraction Tomography Using a Liquid-Electrochemical Transmission Electron Microscopy Cell for Crystal Structure Determination of Cathode Materials for Li-Ion batteries. *Nano Lett.* **2018**, *18*, 6286–6291. [CrossRef]
17. Hadermann, J.; Abakumov, A.M. Structure solution and refinement of metal-ion battery cathode materials using electron diffraction tomography. *Acta Crystallogr. Sect. B Struct. Sci. Cryst. Eng. Mater.* **2019**, *75*, 485–494. [CrossRef] [PubMed]
18. Hadermann, J.; Abakumov, A.; Van Rompaey, S.; Perkisas, T.; Filinchuk, Y.; Van Tendeloo, G. Crystal structure of a lightweight borohydride from submicrometer crystallites by precession electron diffraction. *Chem. Mater.* **2012**, *24*, 3401–3405. [CrossRef]

19. Orlova, E.D.; Savina, A.A.; Abakumov, S.A.; Morozov, A.V.; Abakumov, A.M. Comprehensive Study of Li+/Ni2+ Disorder in Ni-Rich NMCs Cathodes for Li-Ion Batteries. *Symmetry* **2021**, *13*, 1628. [CrossRef]
20. Zhao, H.; Krysiak, Y.; Hoffmann, K.; Barton, B.; Molina-Luna, L.; Neder, R.B.; Kleebe, H.-J.; Gesing, T.M.; Schneider, H.; Fischer, R.X.; et al. Elucidating structural order and disorder phenomena in mullite-type $Al_4B_2O_9$ by automated electron diffraction tomography. *J. Solid State Chem.* **2017**, *249*, 114–123. [CrossRef]
21. Krysiak, Y.; Barton, B.; Marler, B.; Neder, R.B.; Kolb, U. *Ab initio* structure determination and quantitative disorder analysis on nanoparticles by electron diffraction tomography. *Acta Crystallogr. Sect. A Found. Adv.* **2018**, *74*, 93–101. [CrossRef] [PubMed]
22. Brázda, P.; Palatinus, L.; Klementová, M.; Buršík, J.; Knížek, K. Mapping of reciprocal space of $La_{0.30}CoO_2$ in 3D: Analysis of superstructure diffractions and intergrowths with Co_3O_4. *J. Solid State Chem.* **2015**, *227*, 30–34. [CrossRef]
23. Lanza, A.; Margheritis, E.; Mugnaioli, E.; Cappello, V.; Garau, G.; Gemmi, M. Nanobeam precession-assisted 3D electron diffraction reveals a new polymorph of hen egg-white lysozyme. *IUCrJ* **2019**, *6*, 178–188. [CrossRef]
24. Paulus, A.; Hendrickx, M.; Bercx, M.; Karakulina, O.M.; Kirsanova, M.A.; Lamoen, D.; Hadermann, J.; Abakumov, A.M.; Van Bael, M.K.; Hardy, A. An in-depth study of Sn substitution in Li-rich/Mn-rich NMC as a cathode material for Li-ion batteries. *Dalt. Trans.* **2020**, *49*, 10486–10497. [CrossRef]
25. Proffen, T.; Neder, R.B. DISCUS: A program for diffuse scattering and defect-structure simulation. *J. Appl. Crystallogr.* **1997**, *30*, 171–175. [CrossRef]
26. Neder, R.B.; Proffen, T. *Diffuse Scattering and Defect Structure Simulations: A Cook Book Using the Program DISCUS*; Oxford University Press: Oxford, UK, 2008; Volume 11, ISBN 9780191715563.
27. Palatinus, L. PETS—Program for Analysis of Electron Diffraction Data. Available online: http://pets.fzu.cz/ (accessed on 1 August 2021).
28. Palatinus, L.; Brázda, P.; Jelínek, M.; Hrdá, J.; Steciuk, G.; Klementová, M. Specifics of the data processing of precession electron diffraction tomography data and their implementation in the program PETS2.0. *Acta Crystallogr. Sect. B Struct. Sci. Cryst. Eng. Mater.* **2019**, *75*, 512–522. [CrossRef]
29. Petříček, V.; Dušek, M.; Palatinus, L. Crystallographic Computing System JANA2006: General features. *Z. Krist. Cryst. Mater.* **2014**, *229*, 345–352. [CrossRef]
30. Wojdyr, M. Fityk: A general-purpose peak fitting program. *J. Appl. Crystallogr.* **2010**, *43*, 1126–1128. [CrossRef]
31. Karakulina, O.M.; Khasanova, N.R.; Drozhzhin, O.A.; Tsirlin, A.A.; Hadermann, J.; Antipov, E.V.; Abakumov, A.M. Antisite Disorder and Bond Valence Compensation in Li2FePO4F Cathode for Li-Ion Batteries. *Chem. Mater.* **2016**, *28*, 7578–7581. [CrossRef]
32. Drozhzhin, O.A.; Sumanov, V.D.; Karakulina, O.M.; Abakumov, A.M.; Hadermann, J.; Baranov, A.N.; Stevenson, K.J.; Antipov, E.V. Switching between solid solution and two-phase regimes in the Li1-xFe1-yMnyPO4 cathode materials during lithium (de)insertion: Combined PITT, in situ XRPD and electron diffraction tomography study. *Electrochim. Acta* **2016**, *191*, 149–157. [CrossRef]
33. Mikhailova, D.; Karakulina, O.M.; Batuk, D.; Hadermann, J.; Abakumov, A.M.; Herklotz, M.; Tsirlin, A.A.; Oswald, S.; Giebeler, L.; Schmidt, M.; et al. Layered-to-Tunnel Structure Transformation and Oxygen Redox Chemistry in $LiRhO_2$ upon Li Extraction and Insertion. *Inorg. Chem.* **2016**, *55*, 7079–7089. [CrossRef]
34. Fedotov, S.S.; Khasanova, N.R.; Samarin, A.S.; Drozhzhin, O.A.; Batuk, D.; Karakulina, O.M.; Hadermann, J.; Abakumov, A.M.; Antipov, E.V. $AVPO_4F$ (A = Li, K): A 4 V Cathode Material for High-Power Rechargeable Batteries. *Chem. Mater.* **2016**, *28*, 411–415. [CrossRef]
35. Plana-Ruiz, S.; Krysiak, Y.; Portillo, J.; Alig, E.; Estradé, S.; Peiró, F.; Kolb, U. Fast-ADT: A fast and automated electron diffraction tomography setup for structure determination and refinement. *Ultramicroscopy* **2020**, *211*, 112951. [CrossRef]
36. Cichocka, M.O.; Ångström, J.; Wang, B.; Zou, X.; Smeets, S. High-throughput continuous rotation electron diffraction data acquisition via software automation. *J. Appl. Crystallogr.* **2018**, *51*, 1652–1661. [CrossRef] [PubMed]
37. Wang, B.; Zou, X.; Smeets, S. Automated serial rotation electron diffraction combined with cluster analysis: An efficient multi-crystal workflow for structure determination. *IUCrJ* **2019**, *6*. [CrossRef] [PubMed]
38. Gemmi, M.; La Placa, M.G.I.; Galanis, A.S.; Rauch, E.F.; Nicolopoulos, S. Fast electron diffraction tomography. *J. Appl. Crystallogr.* **2015**, *48*, 718–727. [CrossRef]
39. Gruene, T.; Wennmacher, J.T.C.; Zaubitzer, C.; Holstein, J.J.; Heidler, J.; Fecteau-Lefebvre, A.; De Carlo, S.; Müller, E.; Goldie, K.N.; Regeni, I.; et al. Rapid Structure Determination of Microcrystalline Molecular Compounds Using Electron Diffraction. *Angew. Chemie—Int. Ed.* **2018**, *57*, 16313–16317. [CrossRef]
40. Palatinus, L.; Brázda, P.; Boullay, P.; Perez, O.; Klementová, M.; Petit, S.; Eigner, V.; Zaarour, M.; Mintova, S. Hydrogen positions in single nanocrystals revealed by electron diffraction. *Science* **2017**, *355*, 166–169. [CrossRef]
41. Kolb, U.; Gorelik, T.E.; Mugnaioli, E.; Stewart, A. Structural Characterization of Organics Using Manual and Automated Electron Diffraction. *Polym. Rev.* **2010**, *50*, 385–409. [CrossRef]
42. Kodjikian, S.; Klein, H. Low-dose electron diffraction tomography (LD-EDT). *Ultramicroscopy* **2019**, *200*, 12–19. [CrossRef] [PubMed]
43. Steciuk, G.; David, A.; Petříček, V.; Palatinus, L.; Mercey, B.; Prellier, W.; Pautrat, A.; Boullay, P. Precession electron diffraction tomography on twinned crystals: Application to $CaTiO_3$ thin films. *J. Appl. Crystallogr.* **2019**, *52*, 626–636. [CrossRef]

44. Mohanty, D.; Huq, A.; Payzant, E.A.; Sefat, A.S.; Li, J.; Abraham, D.P.; Wood, D.L.; Daniel, C. Neutron Diffraction and Magnetic Susceptibility Studies on a High-Voltage $Li_{1.2}Mn_{0.55}Ni_{0.15}Co_{0.10}O_2$ Lithium Ion Battery Cathode: Insight into the Crystal Structure. *Chem. Mater* **2013**, *25*. [CrossRef]
45. Mosbah, A.; Verbaere, A.; Tournoux, M. Phases LixMnO2λ rattachees au type spinelle. *Mater. Res. Bull.* **1983**, *18*, 1375–1381. [CrossRef]
46. Simancas, J.; Simancas, R.; Bereciartua, P.J.; Jorda, J.L.; Rey, F.; Corma, A.; Nicolopoulos, S.; Pratim Das, P.; Gemmi, M.; Mugnaioli, E. Ultrafast Electron Diffraction Tomography for Structure Determination of the New Zeolite ITQ-58. *J. Am. Chem. Soc.* **2016**, *138*, 10116–10119. [CrossRef]
47. Smeets, S.; Wang, B.; Cichocka, M.O.; Ångström, J.; Wan, W. Instamatic. Available online: http://doi.org/10.5281/zenodo.1090389 (accessed on 1 August 2021).